Journal of Alloys and Compounds 610 (2014) 575–588

Contents lists available at ScienceDirect

Journal of Alloys and Compounds

journal homepage: www.elsevier.com/locate/jalcom

Thermal annealing-induced formation of ZnO nanoparticles: Minimum strain and stress ameliorate preferred *c*-axis orientation and crystal-growth properties

M.F. Malek [a,b,*], M.H. Mamat [a,b], M.Z. Musa [a], Z. Khusaimi [b,c], M.Z. Sahdan [d], A.B. Suriani [e], A. Ishak [a], I. Saurdi [a], S.A. Rahman [f], M. Rusop [a,b]

[a] NANO-ElecTronic Centre (NET), Faculty of Electrical Engineering, Universiti Teknologi MARA (UiTM), 40450 Shah Alam, Selangor, Malaysia
[b] NANO-SciTech Centre (NST), Institute of Science (IOS), Universiti Teknologi MARA (UiTM), 40450 Shah Alam, Selangor, Malaysia
[c] Faculty of Applied Sciences, Universiti Teknologi MARA (UiTM), 40450 Shah Alam, Selangor, Malaysia
[d] Microelectronics and Nanotechnology – Shamsuddin Research Centre (MiNT-SRC), Universiti Tun Hussein Onn Malaysia (UTHM), 86400 Batu Pahat, Johor, Malaysia
[e] Department of Physics, Faculty of Science and Mathematics, Universiti Pendidikan Sultan Idris (UPSI), 35900 Tanjung Malim, Perak, Malaysia
[f] Low Dimensional Materials Research Centre (LDMRC), Department of Physics, Faculty of Science, Universiti Malaya (UM), 50603 Kuala Lumpur, Malaysia

ARTICLE INFO

Article history:
Received 12 February 2014
Received in revised form 5 May 2014
Accepted 6 May 2014
Available online 15 May 2014

Keywords:
ZnO
Thin films
Sol–gel processes
X-ray diffraction
Strain
Stress

ABSTRACT

Nanocrystalline zinc oxide (ZnO) thin films have been deposited on glass substrates using a sonicated sol–gel dip-coating technique at various thermal annealing (T_a) temperatures. The T_a temperature was varied to range from 300 to 600 °C in intervals of 50 °C in an open atmosphere. To obtain desirable piezoelectric properties, the correlations between T_a and the characteristics of ZnO thin films (crystallisation, optical and electrical behaviour) were investigated. The as-deposited films have large compressive stresses of 0.49 GPa, which relaxed to 0.27 GPa as the T_a temperature increased to 500 °C. Optical parameters, such as optical transmittance, absorption coefficient and energy band gap, have been studied and discussed with respect to T_a. All films exhibit a transmittance above 50% in the visible region. It was found that the compressive stresses in the films cause a decrease in the optical band gap, whereas the tensile stress reveals an incline pattern with the optical band gap. This result corroborated with the crystallinity along the *c*-axis plane. The highest crystallinity value was achieved at the lowest stress value. An identical trend was observed for the resistivity values from the *I–V* measurement. Moreover, an increase in the crystallite size from 10 to 39 nm as the level of T_a increased was noticed. The thickness of the films also decreased when T_a increased, and denser films were obtained as a result. A qualified ZnO thin film with good piezoelectric properties has been prepared using a sonicated sol–gel dip-coating technique with various T_a. Experimental results show that T_a has the greatest influence on the final properties of the ZnO thin films.

© 2014 Elsevier B.V. All rights reserved.

1. Introduction

Zinc oxide (ZnO) is a direct wide band gap ($E_g \sim 3.37$ eV) II–VI semiconductor with a large exciton binding energy of approximately 60 meV. This makes excitons stable even above room temperature [1,2]. Researchers are focused on ZnO because of its attractive properties, which include desirable piezoelectric and optoelectronic characteristics [3]. It is therefore widely used for excitonic optoelectronic applications, such as UV sensors [4,5], solar cells [6,7], light emitting diodes (LED), [8] among others. Moreover, ZnO has been reported to be in a class of nontoxic and bio-compatible materials, making it suitable for use in biomedical applications, antiviral applications, textile additives and surfaces that come into contact with humans [9–11].

To obtain a high quality ZnO thin film, some new methods, including flame transport synthesis (FTS) [12], pulsed electron deposition (PED) [13] and pulsed laser ablation [14], have been developed. A variety of common techniques that include pulsed laser deposition (PLD) [15], chemical vapour deposition (CVD) [16], magnetron sputtering [17–19] and sol–gel techniques [20,21] have also been adopted. With the advantages given by simple processing characteristics, high growth rate, low crystallisation temperature and homogeneity on the molecular level because

* Corresponding author at: NANO-ElecTronic Centre (NET), Faculty of Electrical Engineering, Universiti Teknologi MARA (UiTM), 40450 Shah Alam, Selangor, Malaysia. Tel.: +60 176027671.

E-mail address: firz_solarzelle@yahoo.com (M.F. Malek).

http://dx.doi.org/10.1016/j.jallcom.2014.05.036
0925-8388/© 2014 Elsevier B.V. All rights reserved.

of the mixing of liquid precursors, the sol–gel process is one of the most promising deposition techniques for preparing a small or large area deposition of ZnO thin films at low costs for technological applications. Therefore, it can easily be scaled up in industry. However, the presence of intrinsic defects in ZnO films is inevitable during the deposition processes. Stress and strain have significant effects on the film properties because of defect introductions that include oxygen vacancies and zinc interstitials. Therefore, it is crucial to study and understand the role of strain and stress in ZnO films to provide guidance on defect control.

ZnO film quality is determined by the growth process and also by the thermal annealing (T_a) temperature. T_a is an important parameter that could be defined by the process of applying energy to a material and causing changes in its final properties as a result. T_a is a conventional and effective technique to improve crystal quality and to reduce the intrinsic defects in materials when performed in suitable conditions [22]. Additionally, T_a treatment is applied to alter and relieve the internal stresses and to refine the structure by making it homogenous in addition to smoothing the surface of the material. During the T_a process, dislocations and other structural defects move within the material and adsorption/decomposition may occur at the surface. Therefore, the structure and the stoichiometric ratio of the material will change [23].

Some reports on the effects of T_a temperature on the properties of ZnO thin films are available. Certain researchers have reported on the effects of controlling T_a on the tunability of localised surface plasmon resonance (LSPR) of Au nanoparticles embedded in a ZnO matrix [24]. There have also been studies performed on improving ZnO film crystal quality with stronger intensities and narrower full widths at the XRD peak half maximum (FWHM) after the T_a treatment [25]. Furthermore, the influence of T_a temperature on the structural and optical properties of Mg–Al co-doped ZnO (AMZO) thin films has also been reported [26]. They found that the lattice constants, strain and residual stress are influenced by the use of different T_a temperatures. Besides, they also concluded that the defects of AMZO thin films can be manipulated to obtain the desired optical property by varying the T_a temperature.

Appropriate T_a treatment conditions are essential to obtain high-quality ZnO films because various defect types are induced at high T_a temperatures, which can in turn affect the crystal properties. Hence, to understand the effects of T_a, the properties of ZnO thin films that were annealed at various temperatures were studied to identify the optimum T_a that could be expected to give high efficiency and performance for various electronic device applications. In this research study, ZnO thin films were annealed at temperatures ranging from 300 to 600 °C in ambient conditions. This research focused on investigating the influence of T_a on the preferred *c*-axis orientation and on the crystal-growth properties of the produced ZnO thin films.

2. Experimental procedures

2.1. Materials and preparation of ZnO film

The ZnO precursor solution was obtained by following a procedure reported on in detail by the authors elsewhere [27,28]. The ZnO-sonicated sol–gel was prepared as follows: zinc acetate dihydrate ($Zn(CH_3COO)_2{\cdot}2H_2O$, Merck) was first dissolved in 2-methoxyethanol ($C_3H_8O_2$, Merck) at room temperature. Then, monoethanolamine (MEA; C_2H_7NO, R&M) was added dropwise into the solution as a sol stabiliser. The molar ratio of MEA to zinc acetate was maintained at 1.0, and the concentration of zinc acetate was 0.4 M. The resulting solution was stirred at 80 °C for 1 h to yield a clear and homogeneous solution. Afterwards, the solution was sonicated at 50 °C for 1 h using an ultrasonic water bath (Hwasin Technology Powersonic 405, 40 kHz) that served as the coating solution after being cooled to room temperature. The deposition was usually made 24 h after the solution was prepared to make it more stable.

The ZnO glass substrate was dipped into the coating solution and then withdrawn at rates of 40 mm/min at room temperature. To facilitate film thickness measurements, a section of the substrate was covered by an adhesive tape that was subsequently peeled off after the deposition process. After the dip-coating process, the films were dried at 300 °C for 10 min in a furnace to evaporate the solvent and to remove the organic residuals. The substrates were dipped and withdrawn one at a time before the heating treatment. The procedure from deposition to the heating process was repeated five times before undergoing T_a treatment. To investigate the effects of T_a on the properties of ZnO film, the film was annealed in a furnace operating at different temperatures ranging from 300 to 600 °C under atmospheric conditions. When the furnace was heated to each selected temperature, the sample was put into the furnace and held at the temperature for 1 h.

2.2. Measurements

The ZnO thin film crystal structure properties and phases were investigated using a Bruker AXS D8 Advance X-ray diffractometer (XRD) in a standard θ–2θ Bragg–Brentano geometry configuration with a monochromatic Cu Kα (λ = 0.154 nm) radiation. A 40-kV beam voltage and 40-mA beam current were used. Scan pattern data were collected between 25° and 60° with step lengths of 0.02°. The surface morphology and topography of the films were observed using a ZEISS Supra 40VP field emission scanning electron microscope (FESEM) with an electron beam energy operating voltage of 5.0 kV. The film thickness was measured using a KLA Tencor P-6 profilometer. The sample transmission spectra were measured using a Varian Cary 5000 UV–Vis-NIR spectrophotometer ranging between 300 nm and 1500 nm at room temperature in air with a data interval of 1 nm. The photoluminescence (PL) properties of the synthesised film were measured using a Horiba Jobin Yvon-79 DU420A-OE-325 PL spectrophotometer. A helium–cadmium (He–Cd) excitation laser source with a filter and a wavelength of 325 nm was used. For the electrical characterisation, quadrilateral gold (Au) electrodes were sputtered on the top of ZnO film using hard mask. The sheet resistance through current–voltage (*I*–*V*) measurements were performed under illumination from a 100 mW/cm^2 Bukoh Keiki CEP-2000 solar simulator that was set up with a xenon lamp as a light source and a Keithley 2400 computer-controlled current–voltage source meter. The *I*–*V* curve of the film is determined to verify the appropriateness for use of the deposited films in electronic devices.

3. Results and discussion

3.1. Structural and morphological characteristics

3.1.1. X-ray diffraction

Fig. 1 depicts the typical crystal structure XRD patterns and the nanocrystalline orientation of the ZnO thin films annealed at various T_a temperatures. A prominent (002) ZnO diffraction peak with a hexagonal wurtzite crystal structure is observed for all of the films. Other diffraction peaks at the (100), (101), (102) and (110) planes are weak, indicating the preferential orientation of the *c*-axis perpendicular to the substrate surface. All of the diffraction peaks were indexed to the ZnO hexagonal structure according to JCPDS card no. 00-036-1451. The preferentially oriented thin films along the (002) plane could be the minimisation of the internal stresses of the crystal plane. Usually, films grow to minimise the surface energies of the films while also promoting dense atomic packing. This observation suggests that heterogeneous nucleation readily occurs at the interface between the film and

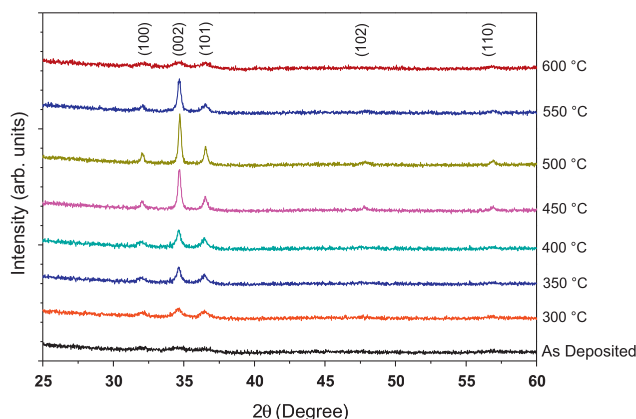

Fig. 1. XRD patterns of ZnO thin films prepared at various T_a temperatures.

the substrate because of surface energy minimisation [29]. The adhesion of the ZnO thin film to the glass substrate was examined by an ordinary tape peel test using 3 M Scotch Tape™. None of the films deposited on glass substrates appeared to be removed, indicating strong adherence of the films to the glass substrates. It is observed that the as-deposited sample exhibits a weak intensity and broad peaks, which indicates poor crystallinity and reveals an amorphous structure of the thin film. Furthermore, as the T_a temperature is increased further to 500 °C, the diffraction intensity of the (002) peak increases by a factor of 3.52 (Table 1), suggesting that T_a at higher temperatures improves the crystallinity quality of ZnO thin films. However, as T_a temperatures increase from 550 °C to 600 °C, the intensity of the *c*-axis orientation decreases. From XRD patterns, we may conclude that for ZnO thin films preheated at identical temperatures, the preferred *c*-axis orientation increases as the T_a temperature increases, and after reaching a peak at certain T_a temperatures, the *c*-axis orientation intensity gradually decreases.

To compare the intensity of the preferred *c*-axis orientation, the relative XRD peak intensity of the film was calculated using the following formula (1) [30]. The relative peak intensity orientation $P_{(hkl)}$ of a particular plane (hkl) can be expressed as follows

$$P_{(hkl)} = \frac{I_{(hkl)}}{\sum I_{(hkl)}} \quad (1)$$

where $I_{(hkl)}$ is the (hkl) peak intensity, and $\Sigma I_{(hkl)}$ is the sum of the intensities of all the diffraction peaks for the ZnO thin film deposited on a glass substrate. The relative peak intensity of the preferred *c*-axis orientation is shown in Table 1. From the calculated values, a relative XRD peak intensity at the (0 0 2) plane increases in the following sample order: $1^* < 8^* < 2^* < 3^* < 4^* < 7^* < 5^* < 6^*$. This suggests that the highest degree of preferred *c*-axis oriented ZnO piezoelectric thin film can be formed by the conditions in the 6^* sample. Higher values of relative peak intensity reveal that the ZnO film crystallinity improves after exceeding certain T_a temperature values. Other research has reported that the ZnO wurtzite hexagonal phase has a natural tendency to grow along the (002) plane, which has a minimum surface energy [31,32]. Therefore, the minimisation of surface energy favours a (002) textured ZnO thin film [33,34].

The average crystallite sizes, *D*, of the films deposited at different T_a temperatures have been calculated using Scherrer's formula (2), which is as follows [35–37]:

$$D = \frac{0.94\lambda}{\beta\cos\theta} \quad (2)$$

where λ, θ and β are the X-ray wavelength (1.54 Å), the Bragg's diffraction angle in degrees and the full width at half maxima (FWHM) of the peak corresponding with the "θ" value in radians, respectively. The average crystallite sizes of the films grown at different T_a temperatures are listed in Table 1. It can be observed that the ZnO thin film crystallite size increased from 10 to 39 nm as the T_a temperature was increased from 300 °C to 600 °C. The merging process of the ZnO nanoparticles induced from T_a temperature can explain this observation. The zinc or oxygen defects at the grain boundaries favour the merging process by stimulating the coalescence of more grains during the T_a process at higher T_a temperatures [38]. Higher T_a temperatures can stimulate the migration of grain boundaries and cause the coalescence of more crystallites during the T_a processes. Small crystallites coalesce together to make larger crystallites and cause larger grain growth. This growth occurs because more energy will be supplied to the atoms so that they may diffuse and occupy the correct sites on the crystal lattice. Grains with lower surface energies will grow larger at higher values of T_a [39].

Table 1
The variation of structural parameters of ZnO thin films at various T_a temperatures.

Sample	Thermal annealing temperature, T_a (°C)	Relative peak intensity (002)	X-ray intensity of diffraction peaks (002) relative to of as-deposited films	FWHM (°)	Crystallite size (nm)
1^*	As deposited	0.265	1.00	0.869	10
2^*	300	0.392	1.48	0.764	11
3^*	350	0.493	1.86	0.513	16
4^*	400	0.532	2.01	0.381	22
5^*	450	0.874	3.30	0.352	24
6^*	500	0.932	3.52	0.298	29
7^*	550	0.763	2.88	0.252	34
8^*	600	0.385	1.45	0.218	39

During most of the synthesis and deposition process, ZnO tends to crystallise in the wurzite phase structure. In this structure, the atomic arrangement of alternating planes is composed of 4-fold tetrahedral coordinated O^{2-} and Zn^{2+} ions stacked alternately along the *c*-axis. The lattice constants *a* and *c* for the ZnO wurtzite structure were calculated according to Braggs law [40]:

$$2d_{hkl}\sin\theta = n\lambda \quad (3)$$

where d_{hkl} is the spacing between lattice planes of Miller indices (*h*, *k* and *l*), *n* is the order of diffraction (usually $n = 1$), λ is the X-ray wavelength of Cu Kα radiation (1.54 Å), and θ is the Bragg's angle (half of the peak position angle). In the ZnO hexagonal structure, the following expression relates the lattice plane spacing to the Miller indices and the lattice constants *a* and *c* [41,42]:

$$\frac{1}{d_{hkl}^2} = \frac{4}{3}\left(\frac{h^2 + hk + k^2}{a^2}\right) + \frac{l^2}{c^2} \quad (4)$$

Thus, for a first order approximation where $n = 1$, the relationship between Eqs. (3) and (4) can be expressed as below:

$$\sin^2\theta = \frac{\lambda^2}{4a^2}\left[\frac{4}{3}(h^2 + hk + k^2) + \left(\frac{a}{c}\right)^2 l^2\right], \quad (5)$$

For the (100) plane orientation, the lattice constant 'a_{film}' is calculated using the following relation [43]:

$$a_{film} = \frac{\lambda}{2\sin\theta}\sqrt{\frac{4}{3}(h^2 + hk + k^2) + \left(\frac{a}{c}\right)^2 l^2}, \quad (6)$$

$$a_{film} = \frac{\lambda}{\sqrt{3}\sin\theta} \quad (7)$$

where θ is the diffracting angle corresponding to the (100) peak. For the (002) plane orientation, the lattice constant c_{film} is determined according the following equation:

$$c_{film} = \frac{\lambda}{2\sin\theta}\sqrt{\frac{4}{3}\left(\frac{c}{a}\right)^2(h^2 + hk + k^2) + l^2}, \quad (8)$$

$$c_{film} = \frac{\lambda}{\sin\theta} \quad (9)$$

The lattice constants a_{bulk} and c_{bulk} for strain-free bulk ZnO are 3.2498 and 5.2066 Å, respectively, as taken from the JCPDS no. 00-036-1451 data card. The lattice parameter values for the ZnO thin films were calculated using Eqs. (7) and (9) and are presented in Table 2. From values obtained in Table 2, it can be observed that the values of c_{film} decrease as the T_a temperature increases. It is believed that lattice contraction contributes to this result [43]. This phenomenon might be a result of the presence of dangling bonds involving Zn^{2+} and O^{2-} ions on the ZnO film surfaces. These

dangling bonds are incompletely coordinated and possess unpaired electrons that form electric dipoles. The boundary layer of each nanoparticle that lies in this surface will contribute to the formation of a parallel array of dipoles and will experience a repulsive force. ZnO has a tendency to absorb O^{2-} and O^{-} ions on the film surfaces. Therefore, the electrostatic attractive interaction between the Zn^{2+} and O^{2-} ions will increase and result in lattice contraction.

In thermally annealed ZnO thin films, it has been observed that the position of the (002) diffraction peak shifted towards the bulk ZnO peak as the T_a temperature increased to 500 °C. This is shown by the XRD stack diagram in Fig. 1. It could be a result of the release of intrinsic strain during the T_a process, indicating the relaxation of the crystal lattice structure and a minimisation of the film surface energy. As T_a temperatures increase from 500 °C to 600 °C, the position of this peak is shifted to an even higher bulk ZnO 2θ value. The shift in the XRD peak (002) towards higher angles as T_a temperature increases has been reported previously by other researchers [44,45]. Furthermore, relative (002) ZnO thin film peak intensity is shown as a function of T_a temperature in Fig. 2. From the XRD analysis, the lattice constant can be further utilised to evaluate the strain, ε_{zz}, in the lattice along the *c*-axis plane. The strain in the ZnO films along the *c*-axis perpendicular to the substrate are calculated using the following formula [46,47]:

$$\varepsilon_{zz} = \frac{c_{film} - c_{bulk}}{c_{bulk}} \times 100\% \qquad (10)$$

where c_{film} is the lattice parameter of the strained films calculated from the X-ray diffraction data, and c_{bulk} is the lattice parameter of ZnO in the bulk (or powder), also called the unstrained lattice parameter. The value of strain is positive (tensile strain) if the material is being stretched and negative (compressive strain) if it is being compressed. It is noted that strain and FWHM gradually decreased with the T_a temperature, as can be observed in Fig. 2. It has also been observed that the strain and FWHM values decrease quasi-linearly as the T_a temperature increases. According to Dhara and Giri, annealing treated samples indicates reduced tensile strain on the annealed ZnO nanostructures [48]. These findings support the reduced pattern of tensile strain with T_a temperature. It can be clearly observed that the decreasing trend in tensile strain values from 0.211% to 0.117% have shown an effective relaxation in the crystal structure as the films are annealed up to a 500 °C T_a temperature. However, increasing the T_a temperature further causes the tensile strain to change to the opposite strain direction (compressive). This indicates the existence of more tense films. These results prove that the previous XRD pattern and the relative peak intensity (002) with the highest *c*-axis orientation were achieved in films that had used a 500 °C T_a temperature. Beyond 500 °C, the (002) orientation intensity peak decreases when the films begin to change the strain direction from a relaxed position to a compressive state of strain. This decrease leads to the formation of more tensed films and of defects in the film crystal structures. This hampered electron movement within the films.

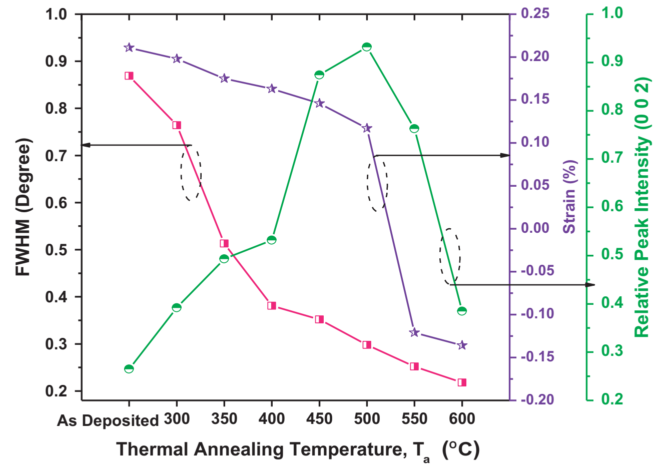

Fig. 2. Variation in the FWHM, strain and relative peak intensity (002) of the ZnO thin films with various T_a temperatures.

To understand the effects of the T_a temperature on the preferred *c*-axis orientation and on the crystal-growth properties, the characteristics of the stress in ZnO films were studied. For hexagonal crystals, the stress, σ_{film}, in the plane of the ZnO films can be determined using the following biaxial stress model expression [49,50]:

$$\sigma_{film} = \frac{2C_{13}^2 - C_{33}(C_{11} + C_{12})}{2C_{13}} \cdot \varepsilon_{zz} \qquad (11)$$

where ε_{zz} is the average uniform lattice strain along the *c*-axis and C_{ij} are the bulk ZnO elastic stiffness constants; i.e., C_{11} = 208.8 GPa, C_{12} = 119.7 GPa, C_{13} = 104.2 GPa and C_{33} = 213.8 GPa [51]. This equation yields the following numerical stress relationship: σ_{film} = -$-233\varepsilon_{zz}$ (GPa). The estimated values of σ_{film} in films grown at different T_a temperatures are listed in Table 2. The sign of the stress indicates whether the films are in a state of compressive or tensile stress. Generally, the total stress in the film consists of two components. First is the extrinsic stress introduced by lattice mismatch and thermal expansion coefficient mismatch between the film and the substrate. The thermal strain is because of the differences in the linear thermal expansion coefficient, α, between hexagonal ZnO ($\alpha_{11} = 6.05 \times 10^{-6}{}^{\circ}C^{-1}$, $\alpha_{33} = 3.53 \times 10^{-6}{}^{\circ}C^{-1}$) and the Corning 7740 glass substrate ($\alpha_{33} = 3.30 \times 10^{-6}{}^{\circ}C^{-1}$) [52]. The substrate exerts a resultant tensile stress effect on the ZnO film as it cools down from higher temperatures to room temperature. This occurs because the thermal expansion coefficient for ZnO is higher than that of the quartz substrate [53,22]. Additionally, the thermal strain introduced by the different linear thermal expansion coefficients, α, of the film and substrate is significantly smaller than the measured strain [54,55]. Secondly is the intrinsic stress, which is associated with defects, impurities and lattice distortions in the crystal structure during the growth process. Most researchers have stated that

Table 2
Lattice parameters, interplane distance, bond length, strain and stress of ZnO thin films at various T_a temperatures.

Thermal annealing temperature, T_a (°C)	Lattice parameters			Interplane distance, d (Å)	Bond length, L (Å)	Strain of *c*-axis (%)	Stress (GPa)
	a_{film} (Å)	c_{film} (Å)	c/a				
As deposited	3.2429	5.2176	1.6089	2.6088	1.9763	0.211	−0.49
300	3.2434	5.2169	1.6085	2.6084	1.9764	0.198	−0.46
350	3.2441	5.2157	1.6077	2.6078	1.9765	0.175	−0.41
400	3.2445	5.2151	1.6074	2.6075	1.9766	0.163	−0.38
450	3.2451	5.2142	1.6068	2.6071	1.9768	0.146	−0.34
500	3.2460	5.2127	1.6059	2.6063	1.9769	0.117	−0.27
550	3.2459	5.2003	1.6021	2.6001	1.9754	−0.121	0.28
600	3.2454	5.1995	1.6021	2.5997	1.9751	−0.136	0.32

the extrinsic stress in thin films normally relaxes as film thickness increases [54,56]. In the present case, thickness varies from 0.82 to 0.16 μm with T_a temperature. Therefore, the extrinsic stress will not be present, and the total estimated stress values seem to be dominantly intrinsic. There are several growth parameters that could contribute to the intrinsic stress, including thermal heating temperature, thermal annealing temperature, deposition time, etc. It shows that the measured film stress is mainly caused by the growth process itself (intrinsic stress) and is not of thermal origin. The residual stress and bond length in the ZnO thin films as a function of T_a temperature is presented in Fig. 3. The observed change in the residual stress of the ZnO thin films was mainly from the T_a and from changes in the defects of the ZnO thin films that result from the change in the bond length (L) of Zn–O in the ZnO films. The following relation gives the bond length of the ZnO films:

$$L = \sqrt{\left(\frac{a^2}{3} + \left(\frac{1}{2} - u\right)^2 c^2\right)} \tag{12}$$

where the u parameter is given by (in wurtzite structures)

$$u = \frac{a^2}{3c^2} + 0.25 \tag{13}$$

which is related to the a/c ratio. The bond length shows an inverse relation with stress as the T_a increased. From the calculated strain in previous calculations, the values of the lattice constant, c, for the as-deposited and annealed films (300–500 °C) are found to be larger compared with the bulk ZnO; the films exhibit tensile strain. The unit cell is elongated along the c-axis, which has been confirmed with the c-lattice and strain values in Table 2. As a result of unit cell elongation, the compressive force acts in the plane of the film. It can be clearly observed that for films deposited at a lower T_a temperature, a strong compressive stress is generated because of structural defects freezing. The adsorbing atoms have too little energy to arrange themselves in their lowest energy states, and intrinsic stresses are therefore built up. During the deposition and growth processes, the crystalline order and structural defects will form at grain boundaries. These defects include dislocations, broken bonds and substoichiometric compositions [57]. All of these defects might induce intrinsic stresses in thin films. At this stage, the magnitude of the compressive stress component is larger than that of the thermal (tensile) stress component [58]. In T_a treatment, some of these defects could be repaired to some degree, and the stress value could decrease accordingly. For a ZnO thin film grown at high T_a temperature, there will be an increment in the atomic mobility that reduces the structural defects because of the high kinetic energy required to grow ZnO. Therefore, a relaxation of stress in ZnO films is observed [59]. Some of the film atoms will also migrate and restructure into thin films when they obtain enough energy in the T_a process. The grains then grow larger correspondingly. A minimum stress of 0.27 GPa is achieved for the highest crystallinity ZnO films annealed at 500 °C, which is nearly free of stress and approaches the value of unstressed bulk ZnO. As discussed before, high c-axis-oriented ZnO thin films are possible because of the free surface energy minimisation on each crystal plane. The existence of the free surfaces will cause missing atom surface bonds. The number of missing bonds will increase with the increment in T_a temperature and contribute to the surface rearrangement to increase atomic bonding. During increases in T_a temperature, the biaxial stress formation will lead to a particular orientation: the (002) orientation [60]. It can be concluded that the compressive stress reduction is consistently accompanied by an enhancement in crystallinity as the T_a temperature is increased up to 500 °C. This will contribute to a lower occurrence of defects and lattice distortions in the crystal lattice structure [61]. The plot in Fig. 3 also reveals that the ZnO thin films exhibit an increase in tensile intrinsic stress when the T_a temperature is too high (550–600 °C). The stress value increases again but in the opposite direction. Similar trends in results have been proposed in situations in which the as-deposited thin films intrinsic stress is compressive stress [62]. They also stated that a T_a process to produce more relaxed films could reduce the compressive stress. However, when T_a temperatures are too high, the tensile stress becomes stronger and eventually exceeds the built-in compressive stress. This leads to a change in the stress direction. This may also be attributed to film thickness variation or to film morphology [55,63].

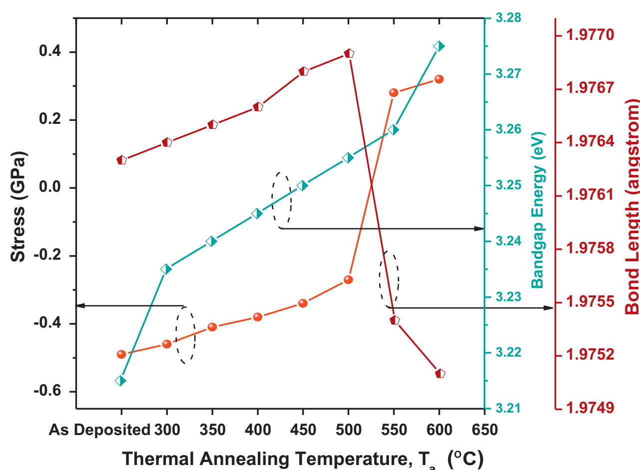

Fig. 3. Variation of the stress, bond length and band gap energy of the ZnO thin films with various T_a temperatures.

3.1.2. Field emission scanning electron microscope (FESEM)

The FESEM morphologies of the ZnO thin films treated at various T_a temperatures are shown in Fig. 4 (50 k magnification; 5 kV applied voltage). T_a plays an important role in the structural and morphological development of the thin film during the deposition process. The influence of the T_a temperature on the crystalline growth can be observed. The grain morphology and formation depends on the interfacial energy acting on the films. Numerous grain boundaries exist, but their size distributions appear to be less homogeneous at lower T_a temperatures. The size difference might also be caused by nonhomogeneous energy distributions that affect the coarsening process. It has also been noted that there are fewer grain boundaries as the grain sizes of the films become larger and that the films feature improved crystallinity with increasing T_a temperatures. High T_a temperature can stimulate grain boundary migration and cause the coalescence of more grains during the T_a process [39]. At higher T_a temperatures, more energy should be available to the atoms so that they may diffuse and occupy the correct sites within the crystal lattice. Therefore, the grains with lower surface energies will grow larger at higher T_a temperatures [64]. The high-magnification images in Fig. 5 (100 k magnification; 5 kV applied voltage) provide supplementary information regarding the thin film structures. The clear evolution from a spherical grain structure (for an as-deposited and annealed film between 300 °C and 400 °C) to a highly faceted granular grain structure (450 °C) can be observed. This granular structure becomes more pronounced at T_a temperatures above 450 °C. Choppali and Gorman proved the existence of this structural transformation at higher T_a temperatures [65]. The increment of intensity values for the (002) plane in the XRD results indicates that the films grew at lower surface energies as the T_a temperature increased [33,66]. However, when the T_a temperature is too high, larger grains grow and result in larger microcracks and a rougher

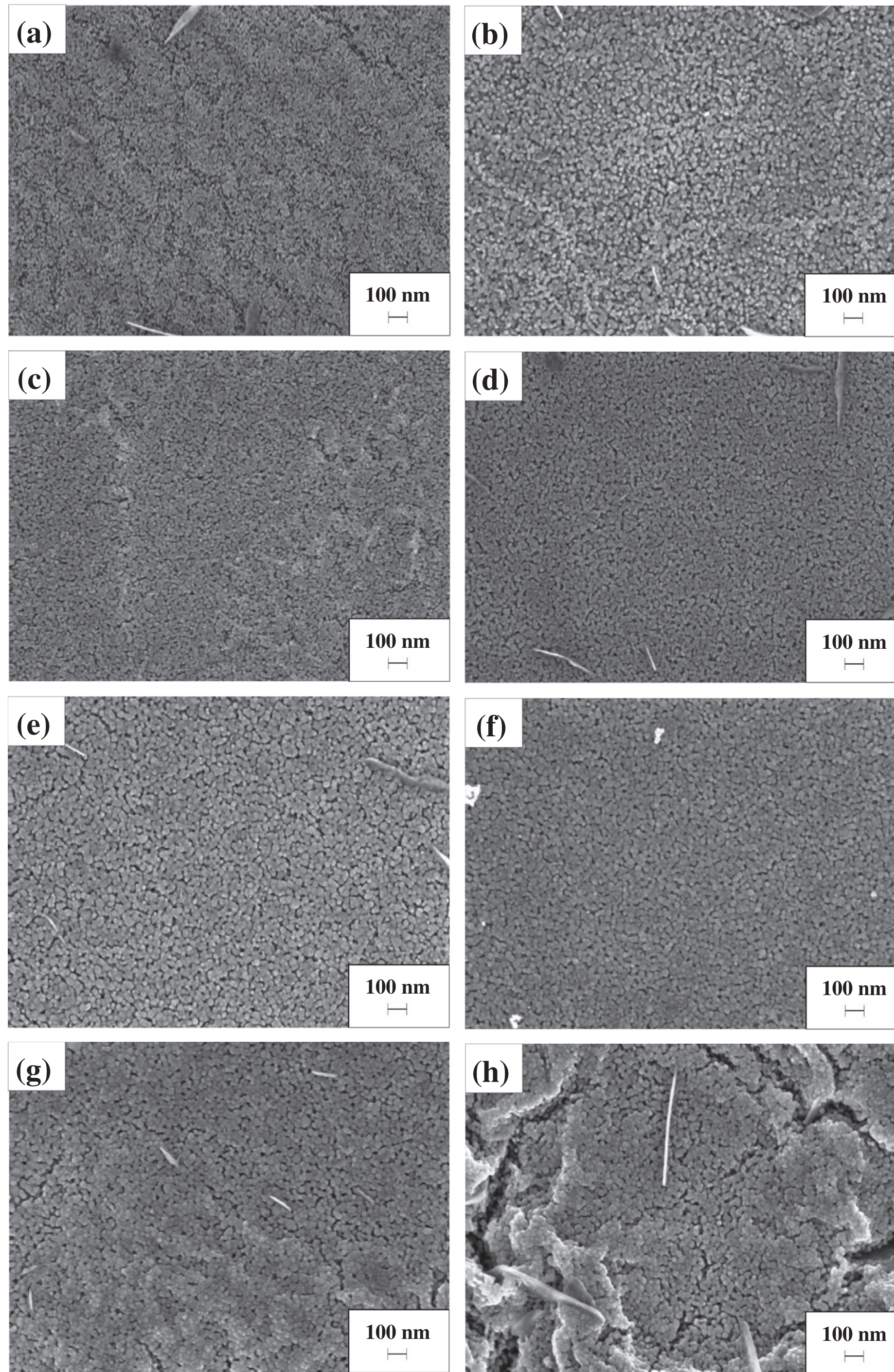

Fig. 4. FESEM morphology of ZnO thin films prepared at various T_a temperatures (50 k magnification; 5 kV applied voltage): (a) as deposited, (b) 300 °C, (c) 350 °C, (d) 400 °C, (e) 450 °C, (f) 500 °C, (g) 550 °C and (h) 600 °C.

surface [49,67]. Figs. 4 and 5(g-h) show the cracks on films annealed at 550 °C and 600 °C. Consequently, this may lead to XRD lower peak intensities and an increase in the film resistivity [49,64]. Additionally, the changes in stress direction beyond 500 °C can be related to the thin film grain size. During the process of raising the T_a temperature from 500 °C to 600 °C, the grain size increases and the small pores within the films combine to form large punctures. The thermal stresses can be released by expanding these punctures. The residual stress is mainly because of the form of the tensile stress at this moment [20]. Furthermore, a decreasing film thickness with increasing T_a temperature was noticed. The film thickness was measured using surface profilometry (KLA Tencor P-6 profilometer) and was found to be in the range of 0.82–0.16 μm. The variation in thickness obtained by the surface profiler is presented in Table 3. This observation is consistent with those from other reports and is a result of increased film density in the case of the higher T_a temperatures [68]. When the as-deposited gel film was subjected to a 300 °C preheating process, ZnO nucleation occurred at the film/substrate interface. The random atomic arrangement in the glass substrate may have disturbed oriented crystal growth in the films. However, the presence of slightly oriented grains can allow oriented grain growth in the second layer

[69]. Therefore, the (002) plane peak intensity increases abruptly. This situation is schematically illustrated in Fig. 6. The structural evolution observed for the cases of various T_a temperatures at fixed preheating temperatures clearly reveals the transition from a granular structure to a columnar one after a certain T_a temperature. During the thin film deposition process, the crystallisation of one layer in a multilayer process is generally affected in an epitaxial-like manner by its preceding layer. Once the first layer was deposited and preheated, homogeneous and heterogeneous nucleation occurred simultaneously. This step was followed by nuclei formation and gradually grew into a crystallite structure. After the first crystallised layer was grown, the grains grew continuously into a newly deposited layer. The nuclei had to be randomly oriented because of the amorphous properties of the glass substrate. Therefore, the crystals were also randomly oriented. Most of the crystallite structure grew preferentially along the (002) direction because of the minimum surface free energy of the material. Only a small part of the crystallite grew along other directions. When the next film layer was deposited, the new crystallites were formed using the preceding layer as a growth template, or seed layer. Therefore, there was some new crystallite still growing in directions other than the (002) direction. This can explain why sample

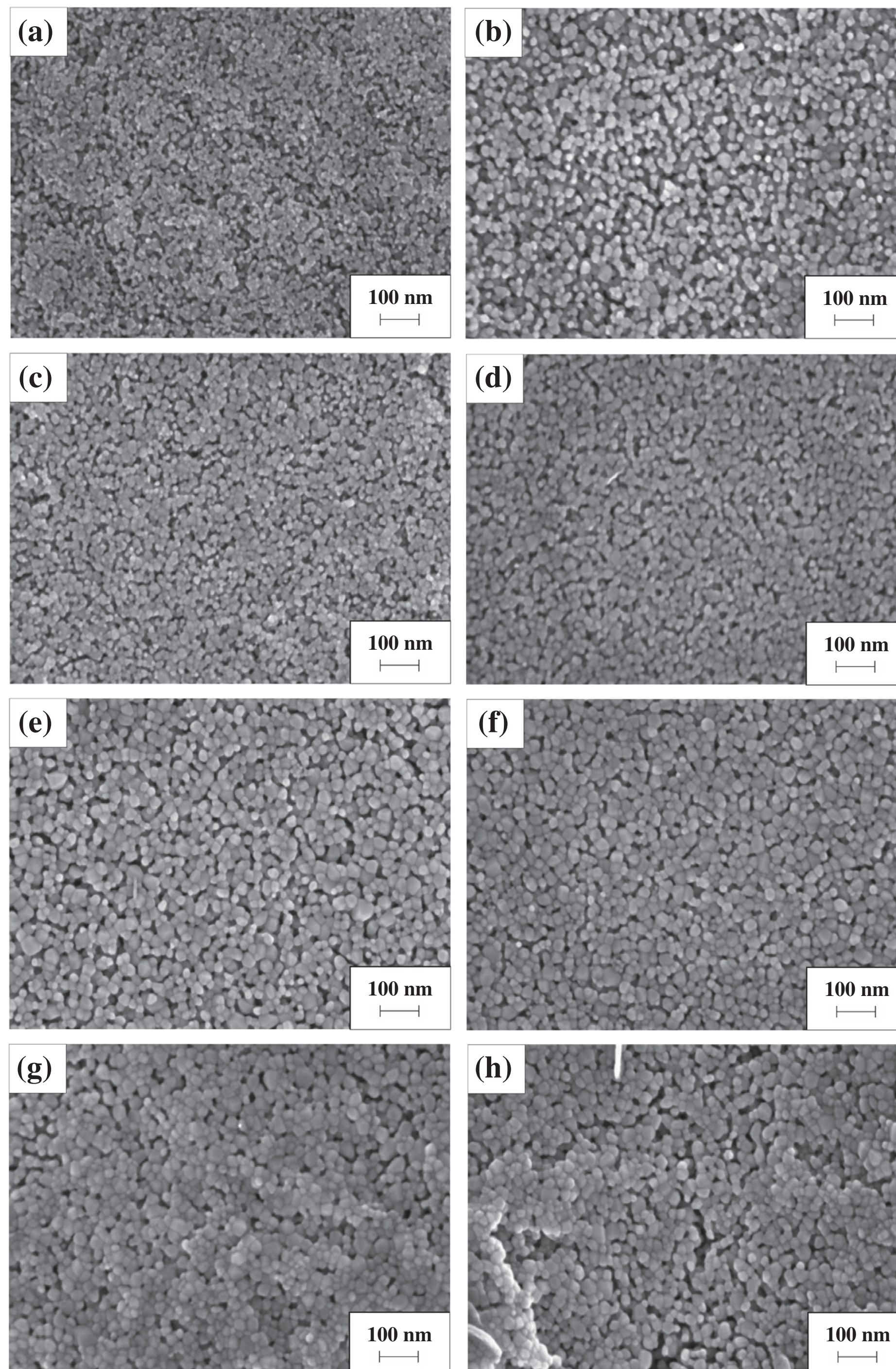

Fig. 5. FESEM morphology of ZnO thin films prepared at various T_a temperatures (100 k magnification; 5 kV applied voltage): (a) as deposited, (b) 300 °C, (c) 350 °C, (d) 400 °C, (e) 450 °C, (f) 500 °C, (g) 550 °C and (h) 600 °C.

Table 3
Thicknesses, average transmittance, optical band gap energy, Urbach energy and porosity of ZnO thin films deposited at various T_a temperatures.

Thermal annealing temperature, T_a (°C)	Thickness (surface profiler) (μm)	Average transmittance (%)	Optical band gap energy (eV)	Urbach energy (meV)	Porosity (%)
As deposited	0.82	54.95	3.215	–	–
300	0.69	58.20	3.235	156	–
350	0.51	58.72	3.240	147	–
400	0.38	58.84	3.245	139	–
450	0.27	68.91	3.250	132	–
500	0.21	90.15	3.255	100	32.89
550	0.18	80.38	3.260	108	6.87
600	0.16	77.56	3.275	125	0.97

A has the (100), (101), (102) and (110) peaks in addition to the (002) peak. After completing the deposition and preheating process, the films were undergoing the T_a process. This is the stage in which the atoms diffuse and migrate between neighbouring layers. When the grains directly contact the neighbouring layer, the coarsening process will occur. Most literature supports the view that the grain structure has no interface between neighbouring layers that evolve into equiaxial ones and that entire single layers can be formed when suitable T_a treatments are used. A suitable treatment includes an appropriately chosen T_a temperature and time [70]. A columnar structure formation through the entire film thickness was formed. This implies that the columnar structure does not necessarily initially develop at the substrate interface but grows through the entire film. To understand the evolution of highly (002) oriented ZnO thin films, a systematic investigation on the growth mechanisms is important and necessary for getting high quality films that will enhance electron transport in the vertical direction, which is important for light harvesting applications for various optoelectronic devices [71].

3.2. Optical properties

3.2.1. UV–Vis-NIR

The optical properties of ZnO thin films are determined using UV–Vis-NIR spectrophotometer measurements between 300 and 1500 nm at room temperature. Fig. 7 shows the transmittance spectra of the films annealed at various T_a temperatures. In all cases, the films are found to be transparent, which is defined as above 50% in the visible-NIR range. It is also observed that the absorption edges are below 400 nm. This is attributed to the intrinsic ZnO band gap because of electron transitions from the valence band to the conduction band. The variation in film thicknesses, which depends slightly on the T_a temperature, improves the transmittance when the T_a temperature increases. The highest transmittance was recorded for a sample annealed at 500 °C with an average transmittance of 90.15% between 400 nm and 800 nm in the visible region, whereas the lowest transmittance was obtained for the as-deposited sample with an average transmittance of 54.95% over the same wavelength. This is shown in Table 3. Generally, the grain boundary produced a larger effect on the properties of the ZnO thin films. From previous FESEM results, the number of grain boundaries decrease when the grains grow larger as the T_a temperature increases. As the T_a process continues, the transmittance spectra increase as film grain boundaries decrease because of better crystallisation and lattice orientation. The improvement in growth along the c-axis at higher T_a temperatures enhances optical scattering reduction in the ZnO thin films. This is believed to be a factor that contributes to the increment in transmittance spectra [72]. However, the thin films annealed at 550 °C and 600 °C show a decrease in transmittance. This may be a result of crystal lattice orientation degradation. Fig. 8 shows the absorption coefficient and α spectra of the ZnO samples annealed at various T_a temperatures. The absorption coefficient was calculated using the previously measured transmittance data. The absorption coefficient, α, was obtained using Lambert's Law, as shown in the following equation:

$$\alpha = \frac{1}{t}\ln\left(\frac{1}{T}\right) \quad (14)$$

where t is the thickness of the thin film, and T is the transmittance of the thin film. The spectra depict an increase in the absorption coefficient in the UV region (<400 nm), which shows the presence of an excitonic nature that is prominent as the T_a temperature increases to 500 °C. This is because of the pattern of strain and stress with an increase in T_a temperature [73]. The increment of

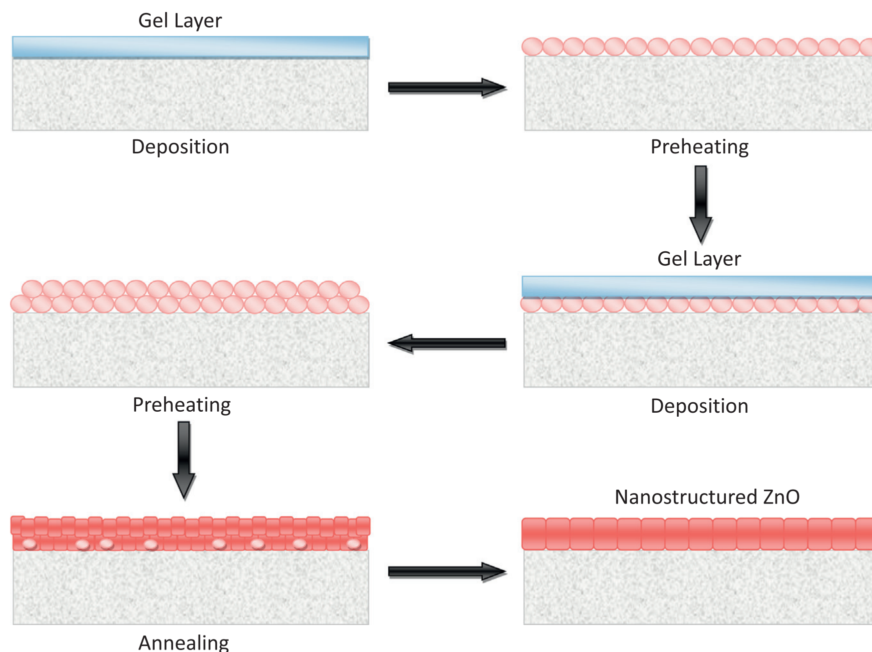

Fig. 6. Schematic of ZnO crystal growth.

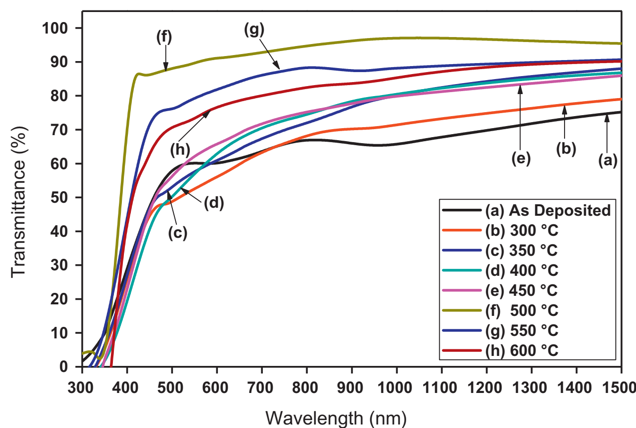

Fig. 7. Transmittance spectra of ZnO thin films prepared at various T_a temperatures as a function of wavelength.

light absorption might be caused by an enhanced optical scattering effect within the ZnO grain boundaries that improves the light absorption in that region [74]. This result corroborates with the improvement in film crystallinity along the preferred *c*-axis plane [27]. However, as the T_a temperature continues beyond 500 °C, a decrement in UV light absorption was observed because of the formation of higher order defects in the ZnO thin films, which occurred as the preferred growth orientations along the *c*-axis plane decreased [29]. The absorption coefficient in the visible-NIR region (400–1500 nm) did not exhibit any significant changes with the T_a temperature. The optical band gap estimation, E_g, of the ZnO thin films deposited at various T_a temperatures using Tauc's plot is shown in Fig. 9. The optical band gap energy, E_g, values in the high absorption region were estimated using the relations given below [75,76]:

$$\alpha h\nu = B(h\nu - E_g)^n \quad (15)$$

$$\alpha h\nu = B\sqrt{h\nu - E_g} \quad (16)$$

where α is the absorption coefficient, $h\nu$ is the photon energy, E_g is the optical band gap, and B is an energy-independent constant with values between 1×10^5 and $1 \times 10^6\ \mathrm{cm^{-1}\ eV^{-1}}$, which depends on electron–hole mobility [76,77]. Values of 1/2, 2, 3/2, and 3 are used for n for allowed direct, allowed indirect, forbidden direct, and forbidden indirect transitions, respectively. For $n = 1/2$, the transition data provides the best linear curve in the band edge region,

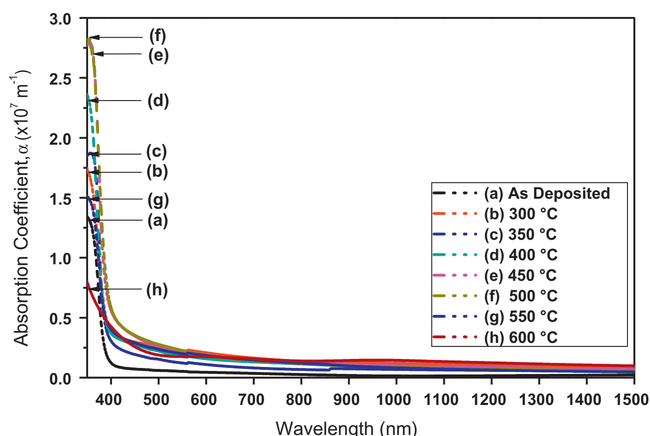

Fig. 8. Absorption coefficient, α, of ZnO thin films prepared at various T_a temperatures as a function of wavelength.

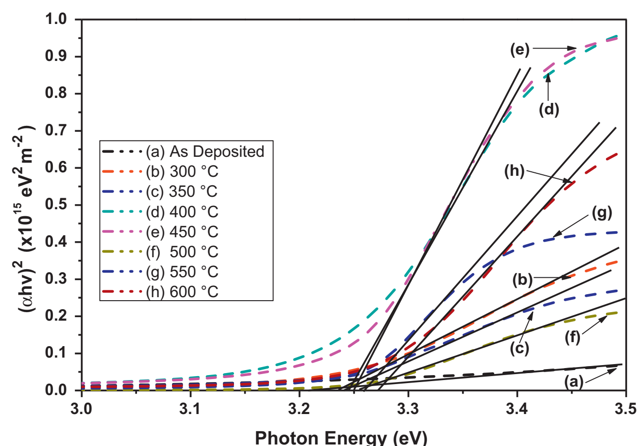

Fig. 9. Estimation of the optical band gap energy, E_g, of ZnO thin films using Tauc's plot as a function of T_a temperatures.

implying that the transition is direct in nature. The absorption coefficient, α, must be assumed to satisfy the equation for a band gap direct material, as shown in Eq. (15), to calculate the band gap energy of the films. The E_g of the ZnO films is obtained by extrapolating the linear part of the curves $(\alpha h\nu)^2$ as a function of the incident photon energy $h\nu$ to intercept the energy *x*-axis. The optical band gap is found to be T_a dependent. The band gap was also found to increase with increases in T_a temperature. From the Tauc's plot, the calculated E_g values ranged between 3.215 and 3.275 eV for all of the films, which is consistent with the published values for the ZnO electronic transition band gap data [78]. The optical band gap energy revealed a blue shift with increasing T_a temperatures. The amount of shift is demonstrated to be dependent on the T_a temperature and may be attributed to the T_a of intrinsic and extrinsic defects. This phenomenon indicates an increment of electron concentrations leading to electron filling at low levels in the conduction band, as explained by the Burstein-Moss effect [79]. The band gap difference between the thin films and the crystal occur because of the existence of grain boundaries and imperfections in polycrystalline thin films. Atomic structures at the grain boundary are different from those within the grain, which leads to larger free carrier concentrations and to the existence of potential barriers at the boundaries. An electric field is therefore formed. This leads to an increase in the band gap [78,80]. The E_g is consistent with the trend in the previously calculated stress. The variations of these parameters are shown in Fig. 3. The strain and stress change the interatomic spacing of semiconductors. This affects the energy gap [81]. The E_g increases as compressive strain/tensile stress along the *c*-axis increases but decreases as tensile strain/compressive stress increases [47,82]. This explains the increase in E_g and the compressive stress decrease when the T_a temperature increases up to 500 °C. On the contrary, when the temperature is greater than 500 °C, the E_g increases because of the increase in tensile stress. Moreover, band gap increase could also be attributed to the evaporation of impurity ions (OH-ions), which lowers the band gap [83]. The compressed lattice is expected to provide a narrower band gap because of the reduced repulsion between the zinc 4s and oxygen 2p bands [47]. This explains why E_g increases and the compressive stress decreases when T_a temperatures increase.

The Urbach energy, corresponding with the tail width of the localised states within the optical band gap, is linked to the absorption coefficient at the lower fundamental edge energy region. The Urbach energy can be determined from the absorption coefficient and depends on structural defects [84]. An estimation of Urbach energy can be used to indicate the presence of various types of

defects in ZnO films. These defects originate during the film growth process, causing lattice disorders and generating stress within the film. The absorption coefficient near the fundamental absorption edge has an exponential dependence on the incident photon energy and obeys the empirical Urbach relation. The equation below represents the exponential shape of the absorption edge in the spectral range of direct optical transitions [85]:

$$\alpha = \alpha_o \exp\left(\frac{hv}{E_u}\right) \quad (17)$$

where α_o is the pre-exponential factor, and E_u is known as the Urbach energy, which is the width of the localised state. Taking the natural logarithm of Eq. (17) yields Eq. (18):

$$\ln \alpha = \ln \alpha_o + \left(\frac{hv}{E_u}\right) \quad (18)$$

Therefore, a plot of $\ln(\alpha)$ against photon energy, hv, should be linear with the Urbach energy as its slope. The Urbach plots of the films are shown in Fig. 10. Urbach energy was calculated from the reciprocal gradient of the linear portion of these curves. The value was included in Fig. 11. It is observed that the Urbach energy reveals a similar pattern of decline with the tensile strain values but that they change inversely with the optical band gap, E_g energy up to 500 °C. As the T_a temperature rises to 500 °C, the atoms gain energy to adjust their positions in the crystal lattice and growth occurs at a lower surface energy, which improves the crystallinity of the films. This result is consistent with the previous XRD analysis. It is also noted that the Urbach energy increases when the T_a temperature is greater than 500 °C. This might be because of the irregular atomic arrangement at higher T_a temperatures during the deposition process, whereby the atoms receive higher energies. This can interrupt the crystal orientation and cause lattice distortion in the films. During the formation of the films, some defects are formed. These defects produce localised states within the films. However, these defects, such as lattice strain and contamination, could be reduced by T_a processes. The Urbach energy initially decreases until the T_a temperature rises to 500 °C. This decrease is caused by the formation of a minimum internal stress within the films that contributes to better atomic arrangement within the crystal structure along the c-axis plane. The Urbach energy increases gradually with T_a temperature beyond 500 °C, indicating the formation of defects. This is supported by the stress and strain increment in the ZnO films, which contribute to disturbances in the lattice orientation along the (002) plane [86]. This explains the breakdown of ZnO crystalline structure at high

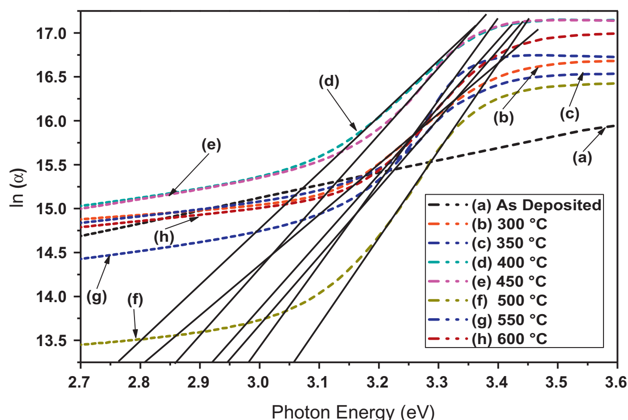

Fig. 10. Plot of $\ln(\alpha)$ versus photon energy for ZnO thin films prepared at various T_a temperatures.

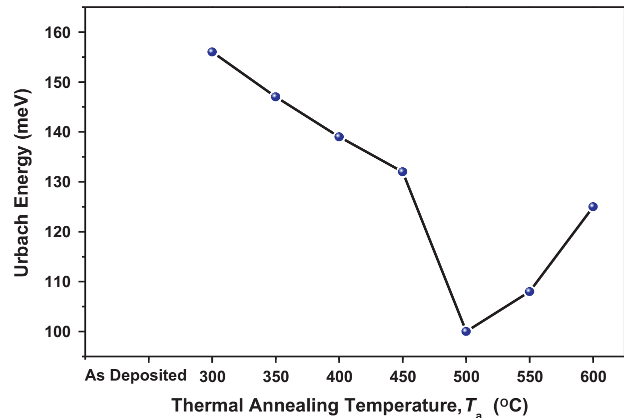

Fig. 11. Urbach energy, E_u, of ZnO thin films as a function of T_a temperatures.

T_a temperatures in the previous XRD spectra. The porosity of the ZnO thin films was estimated using the Lorentz–Lorentz equation below [87,88]:

$$\text{Porosity} = 1 - \left[\frac{[(n_f^2 - 1)/(n_f^2 + 2)]}{[(n_s^2 - 1)/(n_s^2 + 2)]}\right] \quad (19)$$

where n_f is the refractive index of the porous ZnO films, and n_s is the refractive index of the ZnO skeleton, the value of which is widely accepted as 2 [89]. The index of refraction, n_f, at different wavelengths was calculated using the envelope curve for transmittance maxima and transmittance minima in the transmission spectra [90]. The expression for refractive index is given by the following expressions:

$$n_f = \left[N + (N^2 - s^2)^{1/2}\right]^{1/2} \quad (20)$$

$$N = \frac{2s}{T_m} - \left(\frac{(s^2 + 1)}{2}\right) \quad (21)$$

T_m is the envelope function of the transmittance maxima and transmittance minima, and s is the refractive index of the substrate, which is typically 1.52 for the completely transparent glass substrate used in this research [91]. The T_m value is obtained by taking the average of the transmittance data from the transparent region or the region in which the α value is close to 0. This region is between the wavelengths of 400 and 800 nm [92]. The calculated values of porosities for all films are summarised in Table 3. From the table, it is observed that the porosity values have a tendency to decrease when the T_a temperature is in excess of 500 °C. This decrease might be a result of the formation of non-uniform micropores and nanopores within the ZnO crystallite structure. This is common for ZnO prepared by the sol–gel method [92].

3.2.2. Photoluminescence

Fig. 12 shows the room temperature PL spectra of the ZnO films annealed at various T_a temperatures within the wavelength range of 350–700 nm and at an excitation wavelength of 325 nm. It is well known that the luminescence property of ZnO thin films is closely related to the film crystallinity. Normally, the crystallinity is improved when the defect density within the film decreases. The PL spectra in all samples exhibit two main emission peaks. The first is a result of UV emissions, which are near a band edge centred at 380 nm because of free-exciton recombination [93,94]. Second is the deep-level emission, which is beneath the visible region. As the T_a temperature increases to 500 °C, the peak

positions are basically unchanged, but the UV emissions peak intensity increases with the T_a temperature. This result may be attributed to increases in grain size and crystallinity [80]. The strongest UV emissions peak is observed at the highest *c*-axis oriented ZnO film, which is annealed at 500 °C. However, as the T_a temperature increases to 550 °C and 600 °C, the UV emissions peak decreases because of the reduction in crystallinity. It can be suggested that controlling the T_a temperature can enhance the crystallinity of ZnO thin films. This has been confirmed by results from XRD. Green–yellow radiation at the 520–620 nm region was observed for deep-level emissions in the ZnO thin films. It was attributed to structural defects, such as oxygen vacancies (V_o^+) and interstitial oxygen (O_i^-) [95–97]. Additionally, the green–yellow luminescence of ZnO thin films is related to the amount of non-stoichiometric intrinsic defects [98–100]. It originates from the zinc vacancy (V_{zn}) and anti-site defects (O_{zn}) in ZnO films [101]. It is also noted that the biaxial strain and stress in ZnO films only affect the UV emission and do not change the deep level emission intensity.

3.3. Electrical properties

3.3.1. Dark current–voltage (I–V) measurement

The *I–V* characteristics of ZnO thin films deposited at various T_a temperatures are represented in Fig. 13. The sample was attached to a sample holder and placed inside of a dark box. Based on the *I–V* results, all films show ohmic behaviour that obeys Ohm's law: The current through a conductor between two points is directly proportional to the potential difference, or voltage, across the two points. Current will flow and increase in accordance with the magnitude of the voltage applied to the circuit [102,103].

As the applied voltage was increased from −10 to 10 V, the results indicated an increment in current density as the T_a temperature rose to 500 °C. This result may have occurred because ZnO is an *n*-type semiconductor. It is well known that the electrical conductivity of ZnO thin films is generated by defects, such as zinc excess at interstitial positions and by oxygen vacancies. When the T_a temperature is increased to 500 °C, there are interstitial zinc ions in the ZnO crystal structure that decrease the resistivity of the films. However, higher T_a temperatures beyond 500 °C will increase the oxygenation of the interstitial zinc atoms; therefore, reducing the number of interstitial zinc ions will contribute to increasing the resistivity of the films. The roles of the T_a temperature on the sheet resistivity and on the ZnO film conductivity were further investigated. The resistivity and conductivity were

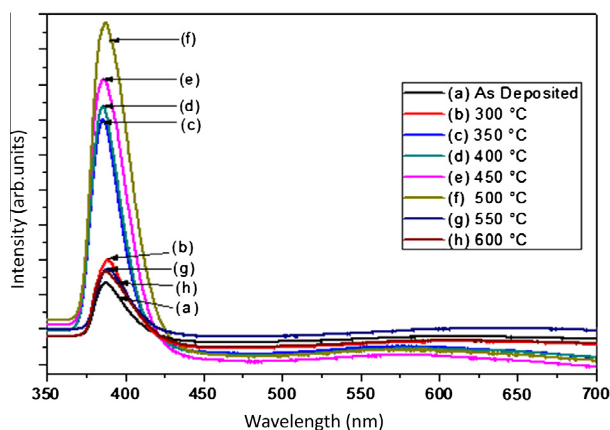

Fig. 12. Photoluminescence spectra of the ZnO thin films as a function of T_a temperatures.

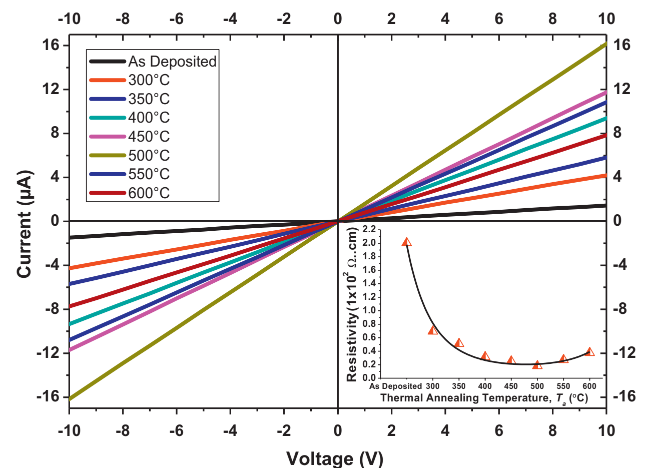

Fig. 13. Dark *I–V* characteristic curves of the ZnO thin films prepared at various T_a temperatures. The inset shows the variation in resistivity as a function of T_a temperatures.

calculated from the slopes of the linear *I–V* plot using the following formulas:

$$\rho = \left(\frac{V}{I}\right)\frac{wt}{l} \tag{22}$$

$$\sigma = \frac{1}{\rho} \tag{23}$$

where V is the supplied voltage, I is the measured current, w is the electrode width, t is the film thickness, l is the length between the electrodes and σ is the film conductivity. The inset in Fig. 13 shows the variation in resistivity in the dark with respect to the T_a temperature. The variation was measured at room temperature. The results show that the electrical resistivity of the thin films decreases when the T_a temperature increases to 500 °C. This result suggests an increase in electron concentrations and electron mobility at higher T_a temperature, which decreases the resistivity of the ZnO thin films. The crystallinity will also affect the resistivity of the film. The crystallinity improvement and orientation of the thin films may decrease the effect of grain boundaries and therefore decrease resistivity. During the T_a process, the energy supplied assists in the diffusion of atoms absorbed on the substrate and accelerates the migration of atoms to favourable energy positions [104]. Higher T_a temperature will induce higher energy supply for atoms during the rearrangement process. However, the atomic arrangement will become disordered if the supplied energy is too high, possibly interrupting the crystal orientation of the thin films. Additionally, the precursors are more completely decomposed and oxidised at higher T_a temperatures and therefore form better ZnO film stoichiometry. The defects that can produce donor levels is decreased, thereby affecting the decrease of carrier concentration [105]. This phenomenon will contribute to the reduction in conductivity in thin films.

3.3.2. Bias current–voltage (I–V) measurement

For the photoconductivity measurement, a 100 mW/cm^2 white bias Xenon lamp was used as a photoexcitation light source. A bias voltage from −10 to 10 V was supplied using a Keithley 2400 source measurement unit, and the resistivity was then measured. The ZnO photoresponse consists of two parts [106]. The first part involved the rapid process of photogeneration and the recombination of electron hole pairs. The second part consisted of a slow process attributed to the oxygen adsorption and desorption on the film surface and the grain boundaries. Generally, ZnO thin films

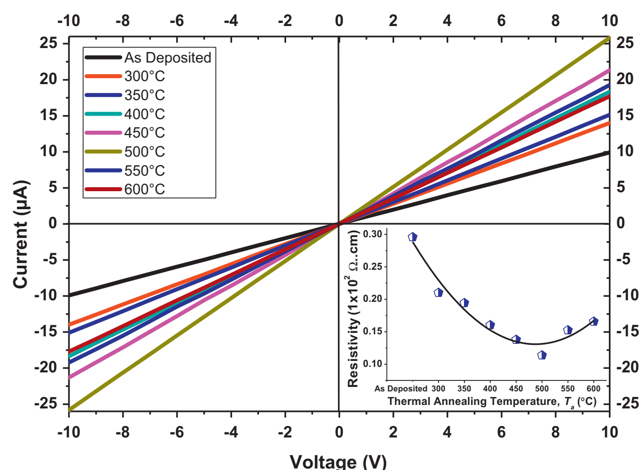

Fig. 14. Bias I–V characteristic curves of the ZnO thin films prepared at various T_a temperatures. The inset shows the variation in resistivity as a function of T_a temperatures.

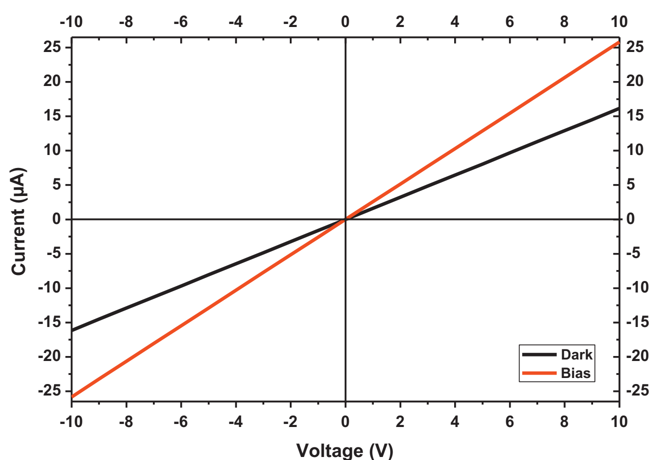

Fig. 15. Dark and photo-illuminated I–V characteristics for ZnO thin films at a T_a temperature of 500 °C.

show n-type conduction because of oxygen deficiencies and interstitial zinc ions. These act as donors in the ZnO lattice. It is well known that the adsorption and desorption of oxygen on the surface and on the grain boundaries is crucial to the decrease and increase in conductivity for ZnO polycrystalline thin films [107]. In the dark, oxygen in air was adsorbed onto a ZnO surface by capturing free electrons from the film, leaving a depletion region near the surface and the grain boundaries. The mechanism of oxygen adsorption is explained with the reaction below [108,109]:

$$O_2(g) + e^- \rightarrow O_2^-(ad) \quad (24)$$

where O_2 is an oxygen molecule, e^- is a free electron, and O_2^- is an adsorbed oxygen ion on the ZnO surface. The negative oxygen ions adhere to the surface and the crystallite interfaces of the film, forming a chemically adsorbed surface state. The negative oxygen ions were not free carriers and could not contribute to the film conductivity. The oxygen adsorption also introduced a potential barrier, which was unfavourable for the carrier mobility. This resulted in lower ZnO conductivity. When under bias light illumination, electron and hole pairs were produced according to following equation:

$$h\nu \rightarrow e^- + h^+ \quad (25)$$

where $h\nu$ is the photon energy, and e^- and h^+ are a photogenerated electron and hole, respectively. Photogenerated holes were captured by the negatively charged oxygen ions to produce oxygen molecules. These molecules desorbed from the ZnO surface and left excess conduction band electrons. The reaction of the oxygen desorption process is described using the equation below:

$$h^+ + O_2^-(ad) \rightarrow O_2 \quad (26)$$

The neutralisation prevented holes from recombining with electrons and increased the life of photogenerated electrons, causing an accumulation of conduction electrons. Therefore, the carrier density increases. The oxygen photodesorption also lowered the barrier height of the grain-boundaries and increased the carrier mobility. Because of the supplied bias voltage, the free carriers moved towards the electrodes to produce a photocurrent. Consequently, conductivity increased. Fig. 14 represents the I–V measurement under white bias light, which revealed an identical pattern to that found under dark I–V. The highest increment of current was achieved at a 500 °C T_a temperature. The inset in Fig. 14 shows the variation in resistivity under bias light illumination with respect to the T_a temperature. The results show an identical pattern to that found in dark conditions, namely that a film displayed the best resistivity when annealed at 500 °C. It is also clearly observed that there is a decrement of electrical resistivity in films annealed beyond 500 °C. The lowest resistivity under bias light illumination is 0.11×10^2 Ω cm. Ohmic behaviour in the I–V curves was observed in the ZnO thin films in the dark and under illumination. It is noted that the current in a given film during voltage application is higher when illuminated than when under dark conditions. This is an indication of the production of electron–hole pairs. The measured dark and photo-illuminated I–V characteristics for ZnO thin film annealed at 500 °C are taken as an example and are shown in Fig. 15. Under 10 V bias, the measured dark current was 16.2 μA. Under white light illumination, photogenerated current was 9.6 μA at a bias of 10 V. The details for other films are summarised in Table 4, in which the average photogenerated current is approximately 9.1 μA. The effects of the light on the films show that the obtained ZnO thin films can be used as photovoltaic materials.

Table 4
Electrical properties of ZnO thin films deposited at various T_a temperatures.

Thermal annealing temperature, T_a (°C)	Dark current (μA)	Photo current (μA)	Photo-generated current (μA)	Resistivity, ρ (1×10^2 Ω cm)		Conductivity, σ (1×10^{-2} S cm^{-1})	
				Dark	Bias	Dark	Bias
As deposited	1.4	9.9	8.5	2.00	0.29	0.49	3.38
300	4.2	14.0	9.8	0.69	0.21	1.44	4.76
350	5.8	15.1	9.3	0.51	0.19	1.96	5.15
400	9.4	18.3	8.9	0.31	0.16	3.18	6.24
450	11.7	21.3	9.6	0.25	0.13	3.99	7.26
500	16.2	25.8	9.6	0.18	0.11	5.49	8.79
550	10.8	19.3	8.5	0.27	0.15	3.68	6.56
600	7.8	17.7	9.9	0.37	0.17	2.65	6.03

4. Conclusions

ZnO nanoparticles with preferred c-axis (002) orientation were synthesised using a sonicated sol–gel dip-coating technique. Based on this research, the T_a temperature is identified to be one of the tremendous factors that control the crystalline quality, crystal lattice orientation, strain, stress, morphology, crystallite and grain size, defects and therefore the physical as well as optical properties of ZnO thin films. As the T_a temperature is increased within the range of 300–500 °C, it favours the formation of highly (002) orientated wurtzite phase ZnO films. The ZnO thin film annealed at 500 °C was the highest (002) oriented along the c-axis plane. The film surface was homogeneous when formed, with dense microstructures that included nano-sized particles. Moreover, increasing the T_a temperature minimised the internal stress/strain and defects within the film. This enhanced electron transport and contributed to a reduction in the resistivity because of the shorter carrier pathway. The as-deposited film, which was initially highly stressed (0.49 GPa), relaxed as T_a was implemented at higher temperatures. Nearly stress- and strain-free ZnO thin films were obtained when annealing at 500 °C before beginning to rise again at higher T_a temperatures. The decrement in the thickness of the film is observed because of the formation of denser crystal structures at higher T_a temperatures. Additionally, the direct band gap variation, E_g, correlated with the stress and strain of ZnO thin films. It is also noted that the film resistivity decreased with T_a, whereas the carrier concentration increased with T_a temperature. This is shown by the PL emission. These results exhibit the interesting properties of ZnO films that result from T_a temperature control. Therefore, good crystalline and strain/stress-free films indicate that ZnO nanoparticles have excellent properties and show promise for use in the fabrication of efficient nano-optoelectronic devices in the near future because of their cooperative behaviour.

Acknowledgements

This work was supported by grant no. 600-RMI/DANA 5/3/PSI (165/2013), 600-RMI/RACE 16/6/2 (9/2013) and by the MyBrain15 programme under the Ministry of Education (MOE). The authors would like to thank the Research Management Institute (RMI), Universiti Teknologi MARA (UiTM), Malaysia for their support. The authors would also like to thank the Faculty of Applied Sciences (UiTM) and the Faculty of Mechanical Engineering (UTHM) for the use of their FESEM and XRD facilities, respectively. The authors thank Mrs. Nurul Wahida (UiTM Asst. Science Officer), Mr. Mohd Azlan Jaafar (UiTM assistant engineer) and Mr. Suhaimi Ahmad (UiTM assistant engineer) for their kind support of this research.

References

[1] M. Zamfirescu, A. Kavokin, B. Gil, G. Malpuech, M. Kaliteevski, Phys. Rev. B 65 (2002) 161205.
[2] Y.K. Mishra, S. Kaps, A. Schuchardt, I. Paulowicz, X. Jin, D. Gedamu, S. Wille, O. Lupan, R. Adelung, KONA Powder Part. J. 31 (2014) 92.
[3] V. Hrkac, L. Kienle, S. Kaps, A. Lotnyk, Y.K. Mishra, U. Schürmann, V. Duppel, B.V. Lotsch, R. Adelung, J. Appl. Crystallogr. 46 (2013) 396.
[4] M.H. Mamat, Z. Khusaimi, M.Z. Musa, M.F. Malek, M. Rusop, Sens. Actuat. A 171 (2011) 241.
[5] M.H. Mamat, M.F. Malek, N.N. Hafizah, Z. Khusaimi, M.Z. Musa, M. Rusop, Sens. Actuat. B 195 (2014) 609.
[6] A.M. Peiró, P. Ravirajan, K. Govender, D.S. Boyle, P. O'Brien, D.D.C. Bradley, J. Nelson, J.R. Durrant, J. Mater. Chem. 16 (2006) 2088.
[7] M.F. Malek, M.Z. Sahdan, M.H. Mamat, M.Z. Musa, Z. Khusaimi, S.S. Husairi, N.D. Md Sin, M. Rusop, Appl. Surf. Sci. 275 (2013) 75.
[8] N. Saito, H. Haneda, T. Sekiguchi, N. Ohashi, I. Sakaguchi, K. Koumoto, Adv. Mater. 14 (2002) 418.
[9] Y.K. Mishra, R. Adelung, C. Röhl, D. Shukla, F. Spors, V. Tiwari, Antiviral Res. 92 (2011) 305.
[10] T.E. Antoine, Y.K. Mishra, J. Trigilio, V. Tiwari, R. Adelung, D. Shukla, Antiviral Res. 96 (2012) 363.
[11] H. Papavlassopoulos, Y.K. Mishra, S. Kaps, I. Paulowicz, R. Abdelaziz, M. Elbahri, E. Maser, R. Adelung, C. Röhl, PLoS ONE 9 (2014) e84983.
[12] Y.K. Mishra, S. Kaps, A. Schuchardt, I. Paulowicz, X. Jin, D. Gedamu, S. Freitag, M. Claus, S. Wille, A. Kovalev, S.N. Gorb, R. Adelung, Part. Part. Syst. Char. 30 (2013) 775.
[13] N.D. Sang, P.H. Quang, D.Q. Ngoc, Commun. Phys. 22 (2012) 65.
[14] C. McLoughlin, P. Hough, J. Costello, E. McGlynn, J.P. Mosnier, Ultramicroscopy 109 (2009) 399.
[15] J.M. Myong, W.H. Yoon, D.H. Lee, I. Yun, S.H. Bae, S.Y. Lee, Jpn. J. Appl. Phys. 41 (2002) 28.
[16] X. Liu, X. Wu, H. Cao, R.P.H. Chang, J. Appl. Phys. 95 (2004) 3141.
[17] O. Kluth, G. Schöpe, J. Hüpkes, C. Agashe, J. Müller, B. Rech, Thin Solid Films 442 (1-2) (2003) 80.
[18] H.S. Al-Salman, A.J. Abdullah, J. Alloys Comp. 547 (2013) 132.
[19] M. Shirazi, M.T. Hosseinnejad, A. Zendehnam, M. Ghoranneviss, G.R. Etaati, J. Alloys Comp. 602 (2014) 108.
[20] M. Wang, J. Wang, W. Chen, Y. Cui, L. Wang, Mater. Chem. Phys. 97 (2006) 219.
[21] D. Fang, K. Lin, T. Xue, C. Cui, X. Chen, P. Yao, H. Li, J. Alloys Comp. 589 (2014) 346.
[22] Y.C. Lee, S.Y. Hu, W. Water, K.K. Tiong, Z.C. Feng, Y.T. Chen, J.C. Huang, J.W. Lee, C.C. Huang, J.L. Shen, M.H. Cheng, J. Lumin. 129 (2009) 148.
[23] J. Yang, M. Gao, Y. Zhang, L. Yang, J. Lang, D. Wang, H. Liu, Y. Liu, Y. Wang, H. Fan, Superlattices Microstruct. 44 (2008) 137.
[24] Y.K. Mishra, S. Mohapatra, R. Singhal, D.K. Avasthi, D.C. Agarwal, S.B. Ogale, Appl. Phys. Lett. 92 (2008) 043107.
[25] J.P. Mathew, G. Varghese, J. Mathew, Chin. Phys. B 21 (2012) 078104.
[26] D. Fang, P. Yao, H. Li, Ceram. Int. 40 (2014) 5873.
[27] M.F. Malek, M.H. Mamat, M.Z. Sahdan, M.Z. Musa, Z. Khusaimi, M. Rusop, Thin Solid Films 527 (2013) 102.
[28] M.F. Malek, M.H. Mamat, Z. Khusaimi, M.Z. Sahdan, M.Z. Musa, A.R. Zainun, A.B. Suriani, N.D. Md Sin, N.D. Md Sin, M. Rusop, S.B. Abd Hamid, J. Alloys Comp. 582 (2014) 12.
[29] S. Suwanboon, Naresuan Uni. J. 6 (2008) 173.
[30] M.J. Alam, D.C. Cameron, J. Vac. Sci. Technol. A 19 (2001) 1642.
[31] N. Fujimara, T. Nishibara, S. Goto, J. Xu, T. Ito, J. Cryst. Growth 130 (1993) 269.
[32] Y. Zhang, H. Zheng, J. Su, B. Lin, Z. Fu, J. Lumin. 124 (2007) 252.
[33] D. Bao, H. Gu, A. Kuang, Thin Solid Films 312 (1998) 37.
[34] L. Xu, X. Li, J. Yuan, J. Nonlinear Opt. Phys. Mater. 17 (2008) 405.
[35] B.D. Cullity, Elements of X-Ray Diffraction, Addison-Wesley Publishing Company Inc., London, 1978.
[36] M.Z. Sahdan, M.H. Mamat, M. Salina, Z. Khusaimi, U.M. Noor, M. Rusop, Phys. Status Solidi C 7 (2010) 2286.
[37] E.F. Keskenler, M. Tomakin, S. Doğan, G. Turgut, S. Aydın, S. Duman, B. Gürbulak, J. Alloys Comp. 550 (2013) 129.
[38] Z.Z. Zhi, Y.C. Liu, B.S. Li, X.T. Zhang, Y.M. Lu, D.Z. Shen, X.W. Fan, J. Phys. D 36 (2003) 719.
[39] Y. Lin, J. Xie, H. Wang, Y. Li, C. Chavez, S. Lee, S.R. Foltyn, S.A. Crooker, A.K. Burrell, T.M. McCleskey, Q.X. Jia, Thin Solid Films 492 (2005) 101.
[40] B.D. Cullity, S. Rstock, Elements of X-ray Diffraction, Prentice Hall, New Jersey, 2001.
[41] T.P. Rao, M.C. Santhoshkumar, Appl. Surf. Sci. 255 (2009) 4579.
[42] D. Gedamu, I. Paulowicz, S. Kaps, O. Lupan, S. Wille, G. Haidarschin, Y.K. Mishra, R. Adelung, Adv. Mater. 26 (2014) 1541.
[43] O. Lupan, T. Pauporté, L. Chow, B. Viana, F. Pellé, L.K. Ono, B. Roldan Cuenya, H. Heinrich, Appl. Surf. Sci. 256 (2010).
[44] X.Q. Wei, Z.G. Zhang, M. Liu, C.S. Chen, G. Sun, C.S. Xue, H.Z. Zhuang, B.Y. Man, Mater. Chem. Phys. 101 (2007) 285.
[45] T. Pauporté, D. Lincot, Electrochim. Acta 45 (2000) 3345.
[46] Selected Powder Diffraction Data for Metals and Alloys, JCPDS, USA 1 (1978) 108.
[47] R. Ghosh, D. Basak, S. Fujihara, J. Appl. Phys. 96 (2004) 2689.
[48] S. Dhara, P.K. Giri, Funct. Mater. Lett. 4 (2011) 25.
[49] Vinay Gupta, Abhai Mansingh, J. Appl. Phys. 80 (1996) 1063.
[50] X.J. Ping, S.S. Bo, L. Lan, Z.X. Song, W.Y. Xin, C.X. Ming, Chin. Phys. Lett. 27 (2010) 047803.
[51] Y.G. Wang, S.P. Lau, H.W. Lee, S.F. Yu, B.K. Tay, X.H. Zhang, K.Y. Tse, H.H. Hng, J. Appl. Phys. 94 (2003) 1597.
[52] J.H. Jou, M.Y. Han, D.J. Cheng, J. Appl. Phys. 71 (1992) 4333.
[53] S.Y. Hu, Y.C. Lee, J.W. Lee, J.C. Huang, J.L. Shen, W. Water, Appl. Surf. Sci. 254 (2008) 1578.
[54] R. Kumar, N. Khare, V. Kumar, G.L. Bhalla, Appl. Surf. Sci. 254 (2008) 6509.
[55] T.P. Rao, M.C.S. Kumar, A. Safarulla, V. Ganesan, S.R. Barman, C. Sanjeeviraja, Phys. B 405 (2010) 2226.
[56] T.B. Hur, Y.H. Hwang, H.K. Kim, I.J. Lee, J. Appl. Phys. 99 (2006) 064308.
[57] H.A. Macleod, Thin-Film Optical Filters, Institute of Physics Pub., 2001.
[58] A. Cimpoiasu, N.M. van der Pers, Th.H. de Keyser, A. Venema, M.J. Vellekoop, Smart Mater. Struct. 5 (1996) 744.
[59] P.R. Berger, K. Chang, P. Bhattacharya, J. Singh, K.K. Bajaj, Appl. Phys. Lett. 53 (1988) 684.
[60] Z. Lixin, H. Hanchen, Appl. Phys. Lett. 90 (2007) 023115.
[61] S.Y. Kuo, W.C. Chen, F.I. Lai, C.P. Cheng, H.C. Kuo, S.C. Wang, W.F. Hsieh, J. Cryst. Growth 287 (2006) 78.
[62] Z.B. Fang, Z.J. Yan, Y.S. Tan, X.Q. Liu, Y.Y. Wang, Appl. Surf. Sci. 241 (2004) 303.
[63] T.P. Rao, M.C.S. Kumar, S.A. Angayarkanni, M. Ashok, J. Alloys Comp. 485 (2009) 413.

[64] Z. Fang, Y. Wang, D. Xu, Y. Tan, X. Liu, Opt. Mater. 26 (2004) 239.
[65] U. Choppali, B.P. Gorman, Opt. Mater. 31 (2008) 143.
[66] T. Ratana, P. Amornpitoksuk, S. Suwanboon, J. Alloys Comp. 470 (2009) 408.
[67] M.K. Puchert, P.Y. Timbrell, R.N. Lamb, J. Vac. Sci. Technol., A 14 (1996) 2220.
[68] M. Ohyama, H. Kozuka, T. Yoko, J. Am. Ceram. Soc. 81 (1998) 1622.
[69] Y. Takahashi, M. Kanamori, A. Kondoh, H. Minoura, Y. Ohya, Jpn. J. Appl. Phys. 33 (1994) 6611.
[70] M.W. Zhu, J.H. Xia, R.J. Hong, H. Abu-Samra, H. Huang, T. Staedler, J. Gong, C. Sun, X. Jiang, J. Cryst. Growth 310 (2008) 816.
[71] W.E. Buhro, V.L. Colvin, Nat. Mater. 2 (2003) 138.
[72] H. Li, J. Wang, H. Liu, H. Zhan, Xia Li, J. Cryst. Growth 275 (2005) e943.
[73] M. Dutta, S. Mridha, D. Basak, Appl. Surf. Sci. 254 (2008) 2743.
[74] K.R. Murali, J. Phys. Chem. Solids 68 (12) (2007) 2293.
[75] J. Tauc, R. Grigorovici, A. Vancu, Phys. Status Solid 15 (1996) 627.
[76] E.A. Davis, N.F. Motta, Philos. Mag. 22 (1970) 903.
[77] S.A.B.S.A. Bux, S.H.A. Aziz, Z.A. Talib, W.M.D.W. Yusoff, Solid State Sci. Technol. 13 (2005) 251.
[78] J. Rodríguez-Báez, A. Maldonado, G. Torres-Delgado, R. Castanedo-Pérez, M. de la L Olvera, Mater. Lett. 60 (2006) 1594.
[79] E. Burstein, Phys. Rev. 93 (1954) 632.
[80] Y.S. Kim, W.P. Tai, S.J. Shu, Thin Solid Films 491 (2005) 153.
[81] J.I. Pankove, Optical Processes in Semiconductors, Dover Publication, New York, 1971. p. 22.
[82] V. Srikant, D.R. Clarke, J. Appl. Phys. 81 (1997) 6357.
[83] F.I. Ezema, U.O.A. Nwankwo, Dig. J. Nanomater. Biosci. 5 (2010) 981.
[84] S. Tanunchai, S. Towta, N. Mangkorntong, P. Mangkorntong, S. Choopun, Chiang Mai J. Sci. 32 (2005) 453.
[85] S. Ilican, M. Caglar, Y. Caglar, J. Optoelectron. Adv. Mater. 9 (2007) 1414.
[86] S.W. Xue, X.T. Zu, W.L. Zhou, H.X. Deng, X. Xiang, L. Zhang, H. Deng, J. Alloys Comp. 448 (2008) 21.
[87] C.J. Brinker, G.W. Scherer, Sol–Gel Science: The Physics and Chemistry of Sol-Gel Processing, Academic Press, New York, 1975. p. 803.
[88] J.H. Yim, J.B. Kim, H.D. Jeong, Y.Y. Lyu, S.K. Mah, J.H. Lee, K.H. Lee, S. Chang, L.S. Pu, Y.F. Hu, J.N. Sun, D.W. Gidley, Mater. Res. Soc. Symp. Proc. 766 (2003) E8.10.1.
[89] G. Wypych, Handbook of Fillers, second ed., Chem Tech. Publishing, Canada, 1999. p. 172.
[90] V. Pandey, N. Mehta, S.K. Tripathi, A. Kumar, J. Optoelectron. Adv. Mater. 7 (2005) 2641.
[91] R. Tricker, Optoelectronics and Fiber Optic Technology, Newnes, Woburn, 2002. p. 39.
[92] S. Mridha, D. Basak, Mater. Res. Bull. 42 (2007) 875.
[93] J.C. Johnson, H. Yan, P. Yang, R.J. Saykally, J. Phys. Chem. B 107 (2003) 8816.
[94] L.E. Greene, M. Law, J. Goldberger, F. Kim, J.C. Johnson, Y. Zhang, R.J. Saykally, P. Yang, Angew. Chem. 115 (2003) 3139.
[95] X.L. Wu, G.G. Siu, C.L. Fu, H.C. Ong, Appl. Phys. Lett. 78 (16) (2001) 2285.
[96] K. Vanheusden, W.L. Warren, C.H. Seager, D.R. Tallant, J.A. Voigt, B.E. Gnade, J. Appl. Phys. 79 (1996) 7983.
[97] X. Jin, M. Götz, S. Wille, Y.K. Mishra, R. Adelung, C. Zollfrank, Adv. Mater. 25 (2013) 1342.
[98] J. Aranovich, A. Oritz, R.H. Bube, J. Vac. Sci. Technol. 16 (1979) 994.
[99] R. Ayouchi, F. Martin, D. Leinen, J.R. Ramos-Barrado, J. Cryst. Growth 247 (2003) 497.
[100] S. Yamauchi, Y. Goto, T. Hariu, J. Cryst. Growth 260 (2004) 1.
[101] J. Wang, L. Gao, Solid State Commun. 132 (2004) 269.
[102] D. Gedamu, I. Paulowicz, S. Jebril, Y.K. Mishra, R. Adelung, J. Nanotechnology 2012 (2012) 325732.
[103] Y.K. Mishra, V.S.K. Chakravadhanula, V. Hrkac, S. Jebril, D.C. Agarwal, S. Mohapatra, D.K. Avasthi, L. Kienle, R. Adelung, J. Appl. Phys. 112 (2012) 064308.
[104] M. Rusop, K. Uma, T. Soga, T. Jimbo, Mater. Sci. Eng. B 127 (2006) 151.
[105] Y. Natsume, H. Sakata, Mater. Chem. Phys. 78 (2002) 170.
[106] X.G. Zheng, Q.S. Li, W. Hu, D. Chen, N. Zhang, M.J. Shi, J.J. Wang, L.C. Zhang, J. Lumin. 122–123 (2007) 198.
[107] S. Jebril, H. Kuhlmann, S. Müller, C. Ronning, L. Kienle, V. Duppel, Y.K. Mishra, R. Adelung, Cryst. Growth Des. 10 (2010) 2842.
[108] X.G. Zheng, Q.S. Li, J.P. Zhao, D. Chen, B. Zhao, Y.J. Yang, L.C. Zhang, Appl. Surf. Sci. 253 (2006) 2264.
[109] L.W. Ji, S.M. Peng, Y.K. Su, S.J. Young, C.Z. Wu, W.B. Cheng, Appl. Phys. Lett. 94 (2009) 203106.